https://doi.org/10.1016/j.ijmecsci.2019.105315

A theoretical and experimental investigation of cutting forces and spring back behaviour of Ti6Al4V alloy in ultraprecision machining of microgrooves

Zejia Zhao[a], Suet To[a,*], Zhiwei Zhu[b,**], Tengfei Yin[a]

[a] State Key Laboratory of Ultra-precision Machining Technology, Department of Industrial and Systems Engineering, The Hong Kong Polytechnic University, Hung Hom, Kowloon, Hong Kong SAR, China

[b] School of Mechanical Engineering, Nanjing University of Science and Technology, Nanjing, J.S, 210094, China

* Corresponding author.

** Corresponding author.

E-mail address: sandy.to@polyu.edu.hk (S. To).

zw.zhu@njust.edu.cn (ZW. Zhu).

A theoretical and experimental investigation of cutting forces and spring back behaviour of Ti6Al4V alloy in ultraprecision machining of microgrooves

Abstract

Studying the material deformation is one of important research foundations in the machining process. In present work, material deformation and spring back behaviour of Ti6Al4V alloy were investigated in ultraprecision machining of seven microgrooves with gradually increased depth of cut to 5 μm. Material constitutive models and geometrical relationships are developed to estimate the temperature evolution, cutting forces, internals force/stress distribution and the spring back variation. The results show that no phase transformation from α to β phase occurs during micro groove machining according to the estimated temperature and experimentally observed microstructures. The calculated cutting forces are in good agreement with the experimental results at various cutting speeds within an error of about 3.53%. Though the increased temperature with the cutting speeds gives rise to low thermal and athermal stresses, the equivalent stress required to overcome the plastic flow of the Ti6Al4V workpiece increases with the speeds due to the high dislocation drag stress. In addition, more than 45% of the thrust force is derived from the spring back force, so the thrust force is significantly affected by the spring back in the machining of Ti6Al4V alloys. The theoretical analysis and experimental results provide potential benefits in predicting the cutting forces and controlling the spring back during machining of Ti6Al4V alloys.

Keywords: Ti6Al4V alloy; Microgrooves; Temperature evolution; Cutting forces; Stresses; Spring back

Nomenclature

F_c Cutting force (N) F_t Thrust force (N)

F_n Normal force exerted on the tool (N) F_n Internal shear deformation force (N)

F_s Spring back force (N)

f_1, f_2 Frictional force of the tool-chip and tool-workpiece (N)

μ_1, μ_2 Frictional coefficients of the tool-chip and tool-workpiece

ψ Equivalent contact angle (°) θ Clearance angle of the diamond tool (°)

α_0 Rake angle of the diamond tool (°) φ Shear angle (°)

l_c Contact length of between the tool and chip (μm)

r_β Edge radius (μm) a_p DoC (μm)

a_t Thickness of the chip (μm) σ_e Equivalent internal stress (MPa)

σ_i Internal stress (MPa) σ_{th}, σ_{ath} Thermal and athermal stress (MPa)

σ_d Dislocation drag stress (MPa) σ_0 Initial stress (MPa)

R Gas constant ($J \cdot mol^{-1} \cdot K^{-1}$) T_j Temperature of the j^{th} chips (K)

ΔG Activation energy ($kJ \cdot mol^{-1}$) ε Shear strain

$\dot{\varepsilon}_0$, $\dot{\varepsilon}$ Reference strain rate and strain rate (s^{-1})

q, p Material constants

h_i Average height of the chip segment at the i^{th} groove (μm)

r_i Radius of the i^{th} groove (μm) w_i Segment width at the i^{th} groove (μm)

w_c Width of cutting chips (μm) r_d Corner radius (μm)

v_s Spindle speed ($r \cdot s^{-1}$)

α_g, α_ρ Constants relating to grain boundaries and dislocation forests

μ Shear modulus (GPa) b Burgers vector (m)

D Average grain size of the workpiece (μm)

ρ Dislocation density (m^{-2}) α_d Dislocation drag coefficient (kPa·s)

f_α, f_β Volume fractions of the α and β phase

T_β β phase transformation temperature (K)

Q Total energy (J) Q_i Absorbed energy of the deformation (J)

Q_t Energy loss between the workpiece and air (J)

Q_r Thermal radiation energy loss (J)

Q_w Energy transferring to the diamond tool (J)

Q_b Energy conduction to the workpiece (J)

n Number of chip segments within the contact region

c Specific heat of the workpiece ($J \cdot kg^{-1} \cdot K^{-1}$)

m_i One segment mass of the serrated chip of the i^{th} groove (kg)

α_a, α_c Heat transfer coefficient of the workpiece-air and the chip-tool ($W \cdot m^{-2} \cdot K^{-1}$)

C_σ Stefan-Boltzmann constant ($W \cdot m^{-2} \cdot K^{-4}$)

k Thermal conductivity ($W \cdot m^{-1} \cdot K^{-1}$) E Young's modulus (GPa)

E_0 Young's modulus at temperature 0 K (GPa) ε_s Elastic strain

1. Introduction

Ti6Al4V alloy has been attracted great attention in astronautic, automobile and biomedical industries due to its high strength to weight ratio and superior corrosion resistance. The alloy is composed of a large amount of α phase with hexagonal closest packing (HCP) crystalline structure and a small amount of β phase with body-centred cubic (BCC) crystalline structure at room temperature[1], so the deformation of the Ti6Al4V alloy is primarily determined by the HCP α phase in the deformation process at relatively low temperature. Since the volume fraction of β phase would be gradually increased with the temperature, the effects of β phase on the deformation of Ti6Al4V alloy should also be considered in the machining process. In comparison to the α phase, the β phase is prone to be deformed in the processing of the two-phase Ti6Al4V alloy. However, the Ti6Al4V alloy is regarded as one of difficult to cut materials in machining due to the rapid tool deterioration and high vibration induced by the favourable chemical reaction between tool and workpiece, low thermal conductivity and inferior elastic modulus.

As the material recovery is highly depended on the elastic modulus in the deformation process, the low modulus could introduce significant spring back after deforming of Ti6Al4V alloy, which affects the desired precision of the workpiece. Since the spring back of materials greatly influences the forming accuracy of the workpiece, understanding the spring back behaviour is important in processing materials. The degree of spring back is significantly affected by many factors, such as the elastic modulus [2], the ratio between grain size and workpiece thickness [3] and

the deformation rate [4]. The elastic modulus is an important parameter to determine the elastic deformation of materials. Generally, the recovery of alloy with high modulus of elasticity is smaller than that with low modulus at the same loading condition according to the Hooke's law [5], so the material recovery varies with the elastic modulus. Liu et al. [6] and Xu et al. [7] reported that the increase in workpiece thickness or decrease in grain size could contribute to a small material spring back during sheet forming. Jiang et al. [4] pointed out that an increase in deformation by altering bending angles could increase the degree of spring back in numerically controlled bending of titanium alloy. Not only spring back occurs in sheet bending with obvious deformation, but also happens in the cutting process. Firstly, the spring back of the alloy might also lead to the workpiece being moved partially away from the cutting tool, which increases the risks of deflection, vibration, and chatter during machining [8]. Furthermore, the cutting and thrust forces are affected by the spring back behaviour during turning [9], milling [10, 11] and fly-cutting [12, 13]. The inevitable spring back of workpiece could generally give rise to an enhancement of cutting forces. In addition, the material recovery could reduce tool marks, which contributes to small surface roughness values in single point diamond turning of ductile materials [14-16].

Prediction of cutting force evolution has been attracted great attention for many years, and the most famous one is the Merchant's force model in orthogonal cutting [17], but the effects of material spring back and cutting tool edge radius are not considered in this model. Arcona and Dow [18] proposed an empirical force model

considering the influence of material elastic deformation and verified their model by diamond turning of four types of metals. Similarly, Zhang et al. [19] reported a force model which considers the tool-workpiece contact area induced by the spring back in vibration-assisted machining. Jun et al. [20] also presented the material spring back in micro-end milling based on the slip-line field cutting force model. The cutting tool edge radius is another important factor to affect the cutting force, especially in ultraprecision machining with small depth of cut (DoC). The effective rake angle tends to be more negative as the depths of cut reach to be comparable to the edge radius [21]. It is generally accepted that materials would be removed by shear deformation if the DoC is larger than the critical chip thickness that is affected by the edge radius, while ploughing instead of cutting would occur if the depth is smaller than the critical chip thickness [22, 23]. Fang [24] predicted the cutting and ploughing forces with respect to the effect of tool edge roundness in machining with a round edge tool. Jin et al. [25] analyzed the stress distribution in the material deformation zone induced by the tool edge radius using the slip-line field model and verified by the cutting forces in micro-turning experiments. Zhu et al [26] and Sun et al [27] proposed an equivalent contact angle induced by the round cutting edge of the diamond tool to successfully predict the dynamic cutting force evolution in turning of the micro-structured surface. Therefore, the effects of spring back and round cutting edge should not be neglected when analyzing the cutting forces in machining metal and alloys.

This study aims to investigate the cutting force evolution with respect to the

material spring back, frictions induced by tool-chip and tool-workpiece, and the round tool edge effect in the machining of Ti6Al4V alloys. The calculated cutting forces are verified by the measured forces in cutting seven microgrooves. Besides, as the spring back is highly affected by the deformation rate with varies with the machining conditions, the amount of spring back of the alloy is also investigated at various depths of cut and speeds.

2. Experimental procedures

Ti6Al4V alloys with a diameter of about 16 mm were utilized for microstructural analysis and microgrooves cutting. The alloy was firstly cut into six samples with a length of about 18 mm by the wire electrical discharge machine, and then all samples were mechanically ground and polished to a relatively flat surface on a series of silicon carbide (SiC) papers and one polishing cloth dispersed by SiC particles with an average size of about 0.5 μm. Half of the samples were chemically etched in a solution with HF: HNO_3: H_2O = 1: 3: 5 for microstructure observation and the others were used for cutting microgrooves.

The rough machining and microgroove cutting were both conducted on a 4-axis ultra-precision machine Moore Nanotech 350FG, as shown in Fig. 1(a). The workpiece Ti6Al4V was fixed on a fixture which is sucked on the vacuum chuck of the machine. A new diamond tool with a corner radius of 1.112 mm, a rake angle of 0°, a front clearance angle of 12.5° and an edge radius of 0.25 μm was applied for the groove cutting. A Kistler 9256C1 force sensor was installed below the tool holder to monitor the cutting and thrust forces. The workpiece was firstly machined by another

diamond tool (corner radius of 1.0002 mm, rake angle of 0° and front clearance angle of 12.5°) to achieve a flat surface, and then finish cutting with a spindle speed of 1000 rpm, DoC of 3 μm and feed of 4 μm/r was carried out twice to further ensure the surface being flat. Finally, seven microgrooves with gradually increased DoC to 5 μm were respectively fabricated at radii of 7 mm, 6 mm, 5 mm, 4 mm, 3 mm, 2 mm and 1 mm of the workpiece with a spindle speed of 600 rpm, and the corresponding cutting speeds v_c are 439.8 mm/s, 377.0 mm/s, 314.2 mm/s, 251.3 mm/s, 188.5 mm/s, 125.7 mm/s and 62.8 mm/s. Fig. 1 (b) schematically illustrates the set-up of finish machining and groove cutting. Three times of the cutting experiment were conducted to ensure reliability.

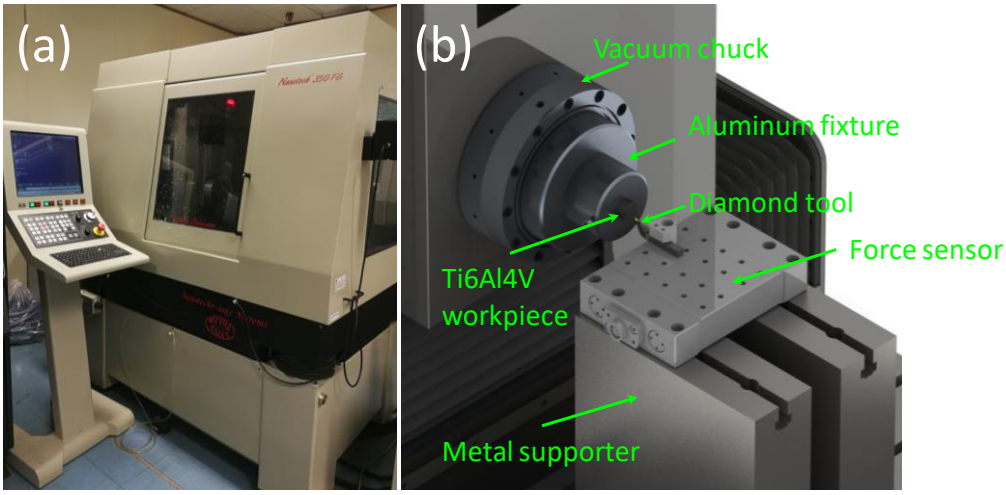

Fig. 1 Ultraprecision machining set-up of (a) a physical image of the Moore Nanotech 350FG and (b) a schematic diagram

A DFC 450 optical microscope (LEICA) was used for microstructure observation. A scanning electron microscope (SEM, Tescan VEGA3) was utilized to detect the electronic morphologies of microgrooves, microstructures and cutting chips. The surface topographies and groove profiles were obtained by a Nexview

three-dimension (3D) optical surface profiler (Zygo).

3. Theoretical models

Fig. 2 (a)-(c) schematically show the forces distribution in the diamond cutting process. An equivalent coordinate system (x_e-y_e) is established to illustrate the frictional force f_1 and the normal force F_n exerted on the tool with consideration of diamond tool edge radius r_β and equivalent contact length l_c between the tool and cutting chip [26]. An equivalent contact angle ψ is used to illustrate the inclined angle of y_e axis from the vertical direction. By considering spring back force F_s, frictional forces f_1 between the tool rake face and chip, and f_2 between the tool flank face and workpiece, the cutting force F_c and thrust force F_t could be expressed to be:

$$\begin{cases} F_c = F_n cos\psi - f_1 sin\psi + f_2 cos\theta \\ F_t = F_n sin\psi + f_1 cos\psi + f_2 sin\theta + F_s \end{cases} \quad (1)$$

where θ is the clearance angle of the cutter. The equivalent contact angle ψ is given by Ref.[26].

$$\psi = \begin{cases} \arccos\left(\frac{l_c}{2r_\beta}\right), & l_c \le l_e \\ \arcsin\left[\frac{r_\beta(1+tan\alpha_0)cos\alpha_0}{l_c}\right], & l_c > l_e \end{cases} \quad (2)$$

$$l_e = \frac{\sqrt{2}r_\beta cos\alpha_0}{\sqrt{1-sin\alpha_0}} \quad (3)$$

where α_0 is rake angle of the diamond tool. According to the slip-line field based model, the contact length l_c could be evaluated as follows[28],

$$l_c = \frac{2a_p cos(\alpha_0-\varphi)}{sin\varphi} \quad (4)$$

where a_p is the DoC and φ is the shear angle between shear direction and cutting speed direction. The shear angle is estimated to be:

$$\varphi = \arctan \frac{\frac{a_t}{a_p} cos\alpha_0}{1-\frac{a_t}{a_p} sin\alpha_0} \tag{5}$$

where a_t is the thickness of the chips. Shear deformation of the workpiece in the primary cutting zone is induced by the force F_n exerted on the workpiece, and the F_n could be obtained by the following equation according to the geometrical relationship shown in Fig. 2 (c).

$$F_n = \frac{F_i + f_1 \sin(\varphi+\psi)}{\cos(\varphi+\psi)} \tag{6}$$

where F_i is the internal force required to overcome plastic deformation of the workpiece, and φ is the shear angle between shear direction and cutting speed direction. The frictional forces f_1 and f_2 are proportional to the normal force and thrust force, respectively.

$$f_1 = \mu_1 F_n, \ f_2 = \mu_2 F_t \tag{7}$$

where μ_1 and μ_2 are the friction coefficients between tool-chip and tool-workpiece, respectively. A moderate value of 0.4 is adopted for the two friction coefficients based on [29]. Consequently, the spring back force F_s could be deduced from Eqs. (1) and (7), as follows:

$$F_s = (1 - \mu_2 sin\theta)F_t - (sin\psi - \mu_1 cos\psi)F_n \tag{8}$$

The internal force F_i contributing to the shear deformation is given by:

$$F_i = \sigma_e A_i = \frac{\sigma_e w_c a_p}{sin\varphi} \tag{9}$$

where σ_e is the equivalent internal stress required to conquer the plastic flow of the

workpiece in the deformation zone, A_i is the area of the shear deformation plane, w_c is the width of cutting chips. Based on the von Mises criterion, the equivalent internal stress is defined as:

$$\sigma_e = \frac{\sigma_i}{\sqrt{3}} \tag{10}$$

where σ_i is the internal stress, which is a sum stress of thermal stress σ_{th}, athermal stress σ_{ath} and dislocation drag stress σ_d at high stress rates, which is expressed by [30]:

$$\sigma_i = \sigma_{th} + \sigma_{ath} + \sigma_d \tag{11}$$

and the thermal stress is evaluated by the Kocks-Mecking model [31, 32]:

$$\sigma_{th} = \sigma_0[1 - \left(\frac{RT_1}{\Delta G} ln \frac{\dot{\varepsilon}_0}{\dot{\varepsilon}}\right)^{\frac{1}{q}}]^{\frac{1}{p}} \tag{12}$$

where σ_0 is the initial stress, R is the gas constant, T_1 is the temperature at the primary deformation zone, ΔG is the activation energy for deformation, $\dot{\varepsilon}_0$ is the reference strain rate, $\dot{\varepsilon}$ is the strain rate during deformation, q and p are material constants. The strain rate is expressed to be:

$$\dot{\varepsilon} = \frac{\varepsilon}{t} \tag{13}$$

where ε and t are the shear strain in the primary deformation zone and time consumed during deformation, which are estimated by [33]:

$$\varepsilon = \frac{cos\alpha_0}{2sin\varphi \cos(\varphi - \alpha_0)} \tag{14}$$

$$t = \frac{h_i}{2\pi r_i v_s} \tag{15}$$

where h_i is the average height of the chip segment, r_i is the radius at i^{th} groove and v_s is the spindle speed.The athermal stress induced by the grain boundaries (σ_g) and dislocations (σ_g) is given by [30]:

$$\sigma_{ath} = \frac{\alpha_g \mu \sqrt{b}}{\sqrt{D}} + \alpha_\rho \mu b \sqrt{\rho} \tag{16}$$

where α_g and α_ρ are constants relating to grain boundaries and dislocation forests, D is the average grain size of the workpiece, and ρ is the dislocation density. Values of the Burgers vector b are 2.95×10^{-10} m and 2.86×10^{-10} for α phase and β phase, respectively. The shear modulus μ is a function of temperature:

$$\mu = 48.66 - 0.032223T_1 \tag{17}$$

At high strain rate (>10^3 s^{-1}) in metal cutting, the dislocation drag stress σ_d could also be one of the internal stresses, as follows [30]:

$$\sigma_d = \alpha_d \dot{\varepsilon} \tag{18}$$

where α_d is the dislocation drag coefficient (α_d = 4.5 kPa·s).

For the Ti6Al4V alloy, the deformation is affected by both α and β phase, so the total required internal stress is [34]:

$$\sigma_i = f_\alpha \sigma_{i,\alpha} + f_\beta \sigma_{i,\beta} + \sigma_d \tag{19}$$

where f_α and f_β are volume fractions of α and β phase, respectively. The sum of f_α and f_β is 1. The content of α phase reduces with temperature, which is given by [35]:

$$\begin{cases} f_\alpha = 0.82\{1 - \exp[0.012(T_1 - T_\beta)]\} & T \le T_\beta \\ f_\alpha = 0 & T \ge T_\beta \end{cases} \tag{20}$$

where $T_\beta = 1268$ K, which is the β phase transformation temperature. The internal stresses $\sigma_{i,\alpha}$ and $\sigma_{i,\beta}$ induced by the α phase and β phase, respectively, could be estimated by the corresponding thermal and athermal stresses, while only thermal stress is considered for the β phase at the temperature above T_β due to the intense recovery at high temperature.

The width of serrated cutting chips could be calculated by the following equation according to the geometry relationship of the diamond tool.

$$w_c = 2\sqrt{r_d^2 - (r_d - a_p)^2} = 2\sqrt{2r_d a_p - a_p^2} \tag{21}$$

From Eqs. (9)-(11), (19) and (21), the internal force F_i can be expressed by:

$$F_i = \frac{2a_p\sqrt{r_d^2-(r_d-a_p)^2}}{\sqrt{3}sin\varphi}\left[f_\alpha\left(\sigma_{i,\alpha}^{th} + \sigma_{i,\alpha}^{ath}\right) + (1-f_\alpha)\left(\sigma_{i,\beta}^{th} + \sigma_{i,\beta}^{ath}\right) + \sigma_d\right] \tag{22}$$

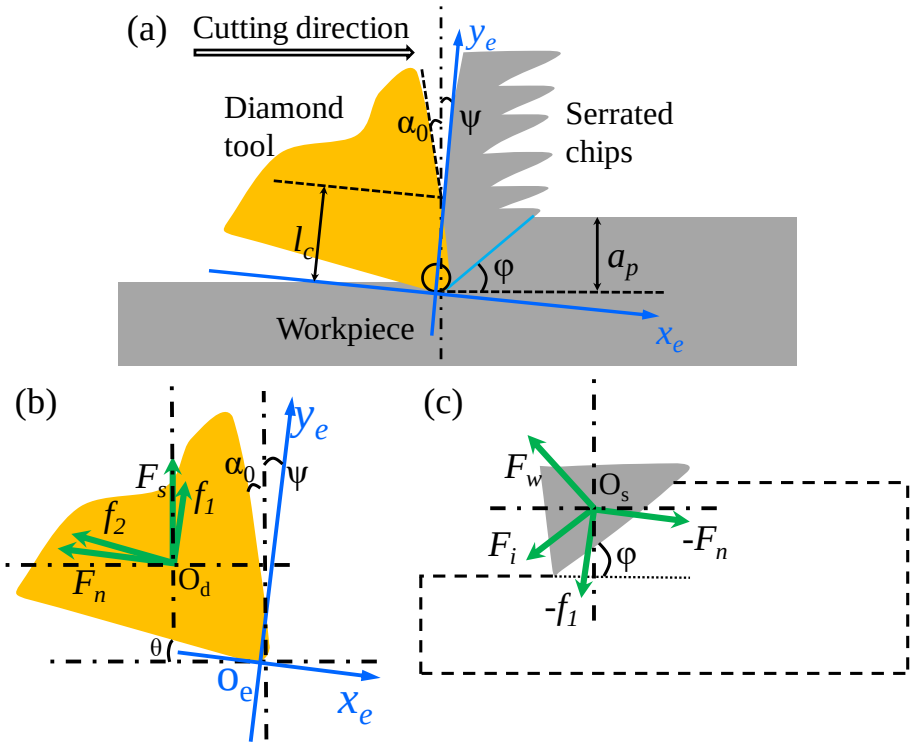

Fig. 2 Schematics of material removal in the ultra-precision groove cutting, (a)

serrated chip formation and force distribution in (b) diamond tool and (c) workpiece

According to the energy conservation law, the total energy Q generated in the shear deformation zone of the workpiece is induced by the work from the force of F_d and f_1, giving:

$$Q = Q_i + Q_t + Q_r + Q_w + Q_b = n(F_n cos\psi - f_1 sin\psi)h_i + (F_n sin\psi + f_1 cos\psi)l_c \cos\psi \quad (23)$$

where Q_i is the absorbed energy in the deformation part, Q_t is the energy loss between workpiece and air, Q_r is the thermal radiation energy loss, Q_w is the energy transferring to the diamond cutting tool, Q_b is heat conduction to the workpiece, and w_i is the average width of the chip segment. An approximate integer value n is the number of chip segments within the contact region between the tool and chip, which is evaluated by the contact length l_c and average chip width w_i at DoC of 5 μm ($n = l_c/w_i$).

One chip segment is supposed to be an independent unit, which means that the temperature of one independent chip segment is the same. Besides, the heat transfer from two adjacent chip segments is not considered. Firstly, the absorbed energy Q_i of chip segments could be evaluated by:

$$Q_i = \sum_{j=1}^{n} cm_i(T_j - T_0) \quad (24)$$

where c is the specific heat of the workpiece (c=560 J·kg^{-1}·K^{-1} [36]), m_i is one segment mass of the serrated chips for the i^{th} groove, T_0 is the room temperature. The energy dissipating to the air is given by [37]:

$$Q_t = \sum_{j=1}^{n} \alpha_a A_1(T_j - T_0)t_j$$

(25)

where α_a is the heat transfer coefficient between workpiece and air, A_1 is the segment area contacting with air, and t is the time that diamond tool passes through the j^{th} chip segment. Furthermore, the energy loss induced by the thermal radiation could be estimated by the Stefan-Boltzmann Law [38]:

$$Q_r = \sum_{j=1}^{n} C_\sigma T_j^4 A_1 t_j$$

(26)

where C_σ is the Stefan-Boltzmann constant ($C_\sigma = 5.67 \times 10^{-8}$ W·m^{-2}·K^{-4}). Besides, the energy transition from chip segments to the diamond tool is evaluated by:

$$Q_w = \sum_{j=1}^{n} \alpha_c A_2 \left(T_j - T_0\right) t_j \quad (27)$$

where α_c is the heat transfer coefficient between the chip segment and diamond cutting tool, and the value is about 2.3×10^5 W·m^{-2}·°C^{-1} [39]. A_2 is the contact area between one segment and the cutter. The heat conduction from the chip segment to the workpiece is evaluated to be [37]:

$$Q_b = \frac{nkA_3(T_1 - T_0)t\cos\varphi}{d_c}$$

(28)

where k is the thermal conductivity of the workpiece and A_3 is the contact area between the segment and workpiece. The temperature T_j at the j^{th} chip segment could be evaluated by the following expression:

$$cm_i T_1 = cm_i T_j + \alpha_a A_1 \left(T_j - T_0\right) t_{j-1} + C_\sigma T_j^4 S t_{j-1} + \alpha_c A_2 \left(T_j - T_0\right) t_{j-1} \quad j \geq 2 \quad (29)$$

A three-dimensional schematic diagram of serrated chips is shown in Fig. 3, which illustrates the features of Ti6Al4V cutting chips, including chip height h_i or

chip thickness, chip width w_c, segment width w_i, and the distance between two chip segments. From the geometrical relationship, the mass the one segment could be calculated by:

$$m_i = \rho_m V_i = \frac{\rho_m w_i h_i w_c}{2} \tag{30}$$

where ρ_m and V_i are workpiece density and one segment volume, respectively. The three contact areas are given to be:

$$\begin{bmatrix} A_1 \\ A_2 \\ A_3 \end{bmatrix} = \begin{bmatrix} \frac{2w_c h_i}{cos\varphi} + w_i h_i \\ w_c w_i \\ \frac{w_c a_p}{cos\varphi} \end{bmatrix} \tag{31}$$

For the j^{th} chip segment, the total time consumed is:

$$t_j = jt = \frac{j h_i}{2\pi r_i v_s} \tag{32}$$

Based on Eqs. (23) - (32), the temperature during shear deformation could be estimated in ultra-precision groove cutting process, and then the cutting force and material spring back force are obtained according to Eqs. (1) and (8), respectively.

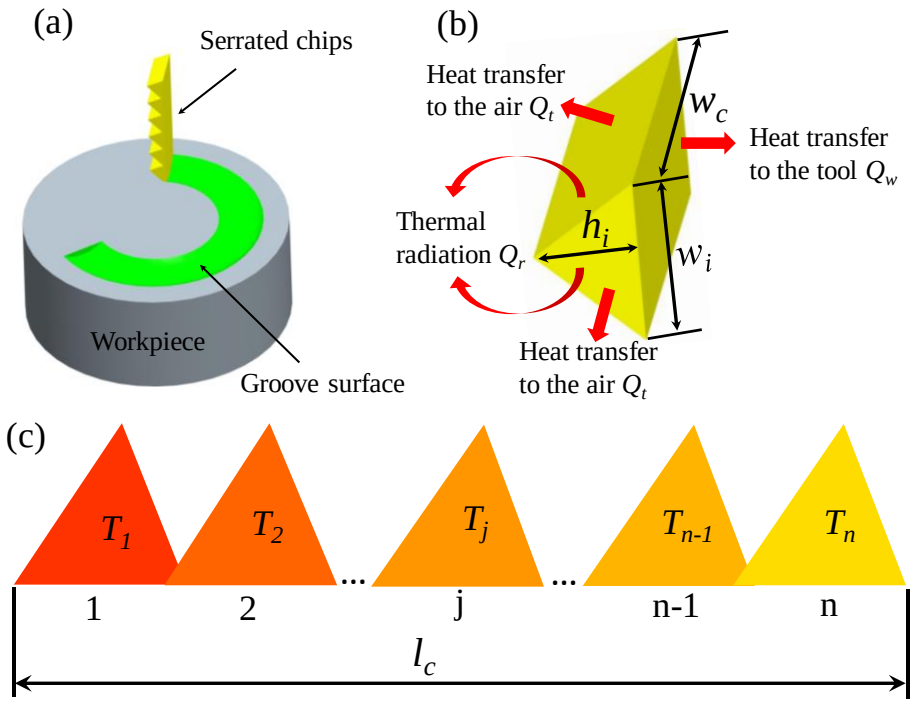

Fig. 3 Serrated chip formation process in groove cutting, (a) a schematic diagram, (b) one segment of serrated chips, and (c) temperature evolution of the serrated chip within contact region between the tool and chip

Fig. 4 (a) and (b) show the SEM morphology and schematic drawing of the diamond cutting tool with conical clearance, respectively. In ultra-precision groove cutting, a fraction of materials under the tool flank face would spring back after the tool passing through the deformation part, as shown in Fig. 4 (c). Blue dashed circles are derived from the measured groove surface profile after materials totally spring back. The workpiece has completely rebounded at point B, so no spring back force is exerted on the diamond cutting tool. In comparison, the pending spring back amount is highest at point A in the rake face of diamond tool, giving rise to the largest elastic recovery force. Therefore, the spring back force and elastic stress show gradient distribution in the flank face of the cutting tool.

Fig. 4 (d) and (e) illustrate the spring back amount with gradient elastic stress

distribution at the rake and flank face of the diamond tool, respectively. As the material spring back shows symmetrical character along the plane of ABE, the component elastic stress would be counteracted in the y-direction. Hence, the component elastic strain in y-direction has no effect on the generation of spring back force. In other words, the spring back force is primarily induced by the component elastic stress in z-direction during groove cutting. Hence, the spring back force induced by material recovery could be expressed by:

$$F_s = A_e \sigma_s = A_e E \varepsilon_s \tag{33}$$

where A_e is the effective area perpendicular to the z-axis, E is the Young's modulus, σ_s and ε_s are the average elastic stress and strain in the z-direction, respectively. According to the geometry relationship, the effective area is calculated as follows:

$$A_e = \frac{w_c h_{BF}}{2tan\theta} \tag{34}$$

where h_{BF} is the height of BF in Fig. 4 (c), which is the difference between ideal cutting profile and measured outline after totally spring back of workpiece. Increase in the height difference could give rise to a high spring back force. The Young's modulus E is a temperature-dependent parameter, which is evaluated by [40]:

$$E = E_0\{1 - \left[\left(\frac{T}{T_m}\right) * exp\left[\theta^* \left(1 - \frac{T_m}{T}\right)\right]\right]\} \tag{35}$$

where E_0, denote the Young's modulus at temperature 0 K, T_m is the melting temperature of Ti6Al4V workpiece, and θ^* represents the characteristic homologous temperature.

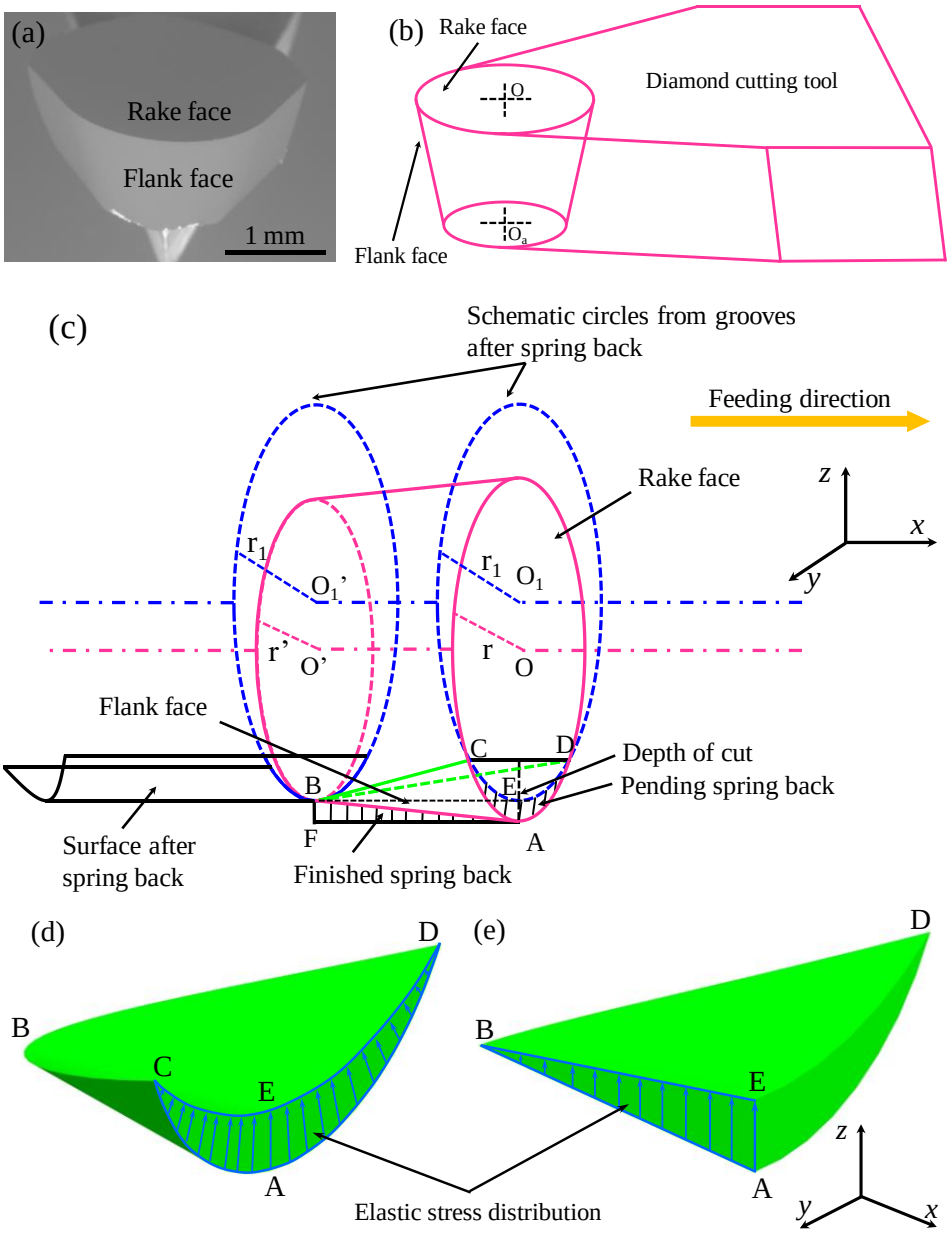

Fig. 4 The diamond cutting tool of the (a) SEM morphology and (b) brief schematic drawing; (c) geometry illustration of material spring back during groove and cutting; elastic stress distribution in (d) rake face and (e) flank face of the diamond tool

4. Results and discussion

4.1 Microstructures of Ti6Al4V alloys and microgrooves

Fig. 5 illustrates the optical and electronic microstructure of the Ti6Al4V alloy with α and β phases at room temperature. The alloy is primarily composed of α phase

with an average grain size of about 3 μm, as shown by the white and dark sites in Fig. 5 (a) and (b), respectively. Some β particles distribute between two neighbouring α phases.

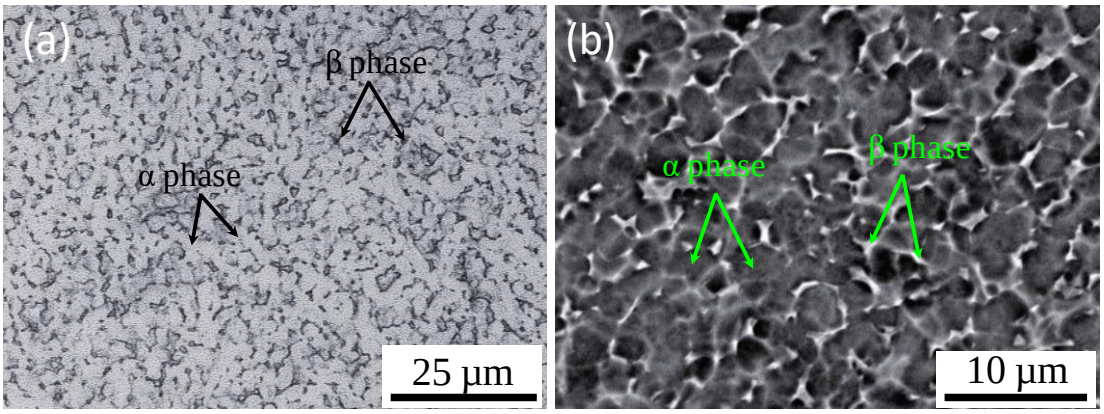

Fig. 5 Microstructures of Ti6Al4V alloys obtained from (a) optical microscope and (b) scanning electron microscope

Seven microgrooves with gradually increased DoC to 5 μm at various radii with an interval of 1 mm are clearly observed in the 3D topography shown in Fig. 6 (a). The radii of the first and seventh grooves are 7 mm and 1 mm respectively. As the seven grooves show similar features, only one magnifying morphology of the 7th groove is shown to demonstrate the groove characteristics, as illustrated in Fig. 6 (b).

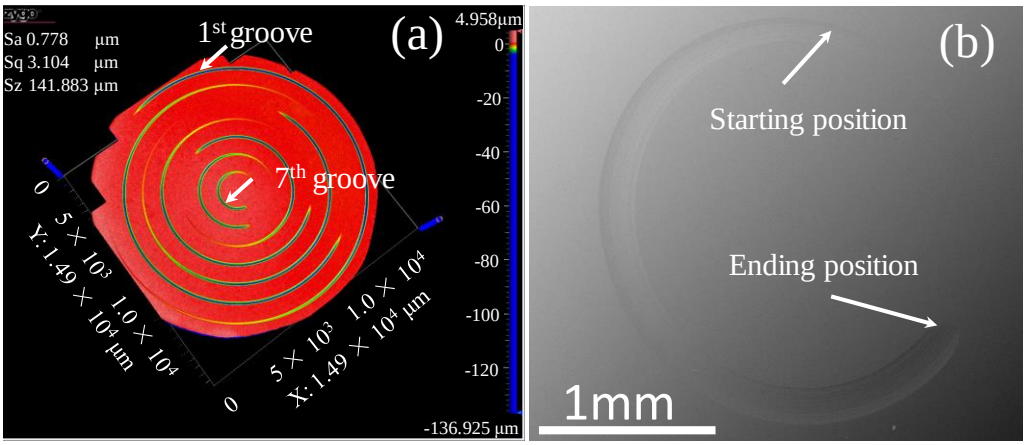

Fig. 6 Groove morphologies obtained from the (a) 3D Zygo profiler and (b) SEM

4.2 Serrated chip features

Chip morphologies of the seven grooves after machining are shown in Fig. 7. Continuous cutting chips could be clearly observed for all grooves after cutting process, which is attributed to the low cutting speeds in comparison to the high speed machining of Ti6Al4V with cutting speeds higher than several tens of meters per second at which condition discontinuous chips could be obtained in machining [41].

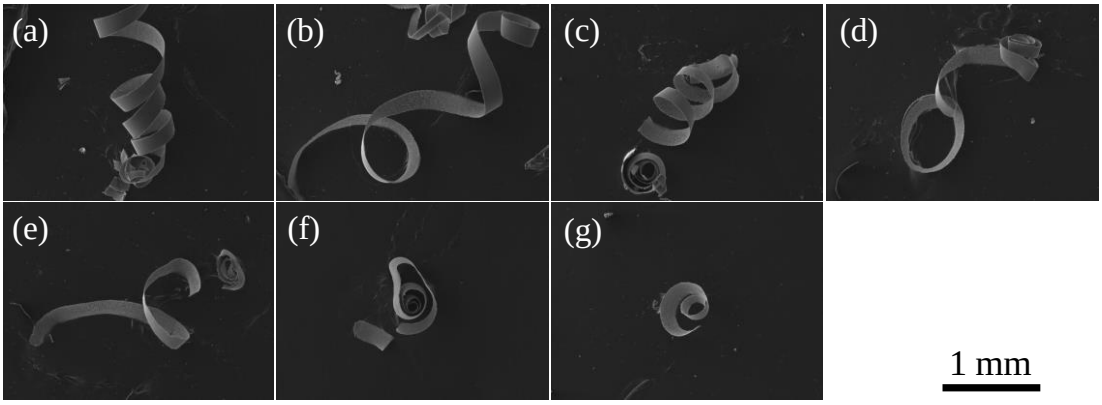

Fig. 7 Continuous cutting chips obtained from grooves at cutting speeds of (a) 439.8 mm/s, (b) 377.0 mm/s, (c) 314.2 mm/s, (d) 251.3 mm/s, (e) 188.5 mm/s, (f) 125.7 mm/s and (g) 62.8 mm/s

One continuous cutting chip is generally composed of a large number of small successive chip segments, as shown in Fig. 8. Typical serrated chips are observed for all grooves even at an extremely low cutting speed of 63 mm/s. However, the distance between two adjacent chip segments varies with grooves. Increase in cutting speed contributes to a distance reduction of two neighbouring segments. Besides, the contact width w_i between the diamond tool and chip segments and segment height h_i are different for various cutting chips, which could be measured from chip morphologies. The average values of w_i and h_i at the DoC of 5μm are listed in Table 1, which are

calculated from at least twenty segments for each of cutting chip. The average measured thrust forces at the depth of 5μm with various cutting speeds are also given in the table.

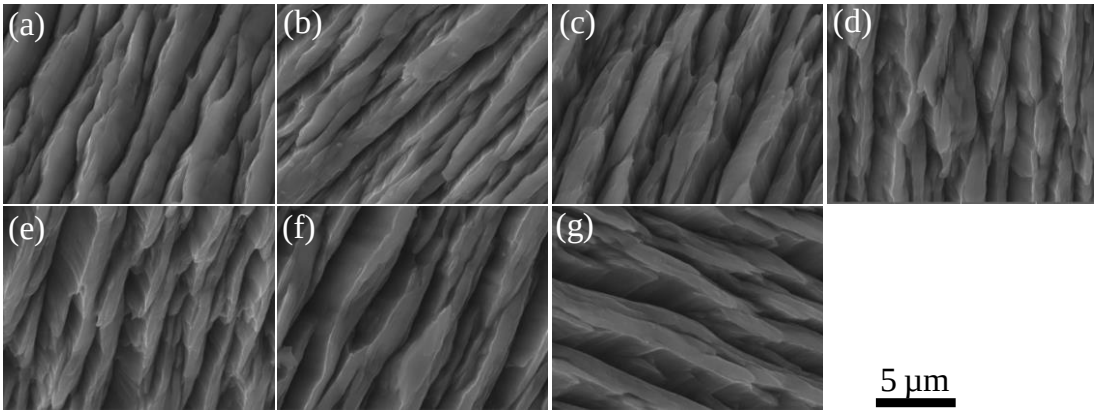

Fig. 8 Serrated chip morphologies of grooves at cutting speeds of (a) 439.8 mm/s, (b) 377.0 mm/s, (c) 314.2 mm/s, (d) 251.3 mm/s, (e) 188.5 mm/s, (f) 125.7 mm/s and (g) 62.8 mm/s

Table 1 Experimental parameters for various microgrooves

Grooves	1st	2nd	3rd	4th	5th	6th	7th
$v_c(\mathrm{mm/s})$	439.82	376.99	314.16	251.33	188.50	125.66	62.83
$w_i(\mu\mathrm{m})$	1.738	1.850	1.921	2.080	2.387	3.125	3.282
$h_i(\mu\mathrm{m})$	3.042	3.081	3.080	3.123	3.120	3.285	3.856
$\dot{\varepsilon}_i\times10^{-4}$ (s^{-1})	9.398	7.909	6.594	5.171	3.883	2.407	0.973
F_t (N)	1.823	2.017	2.173	2.206	2.242	2.243	2.245

4.3 Temperature evolution in micro groove cutting

As the deformation of the workpiece is significantly affected by the temperature, it is meaningful to obtain the temperature during machining different grooves. However, the temperature of the deformation zone is difficult to be directly measured

in the machining process, so the evolution of temperature is estimated according to the geometry and physical models given in Section 3. Relevant parameters from previous research are tabulated in Table 2.

Table 2 Parameters for models calculation

Parameter	Value	Ref.	Parameter	Value	Ref.
$\sigma_{0,\alpha}$ (MPa)	1078.6451	[34]	q_β	1	[42]
$\dot{\varepsilon}_{0,\alpha}$ (s^{-1})	10^{17}	[34]	p_β	0.4	[42]
ΔG_α ($kJ \cdot mol^{-1}$)	560.2436	[34]	α_g	0.4544	[30]
q_α	1.1131	[34]	α_ρ	0.5	[30]
p_α	0.3189	[34]	ρ (m^{-2})	10^{12}	[30]
$\sigma_{0,\beta}$ (MPa)	1200	[42]	k ($W \cdot m^{-1} \cdot K^{-1}$)	7.0	[43]
$\dot{\varepsilon}_{0,\beta}$ (s^{-1})	2×10^{13}	[42]	α_a ($W \cdot m^{-2} \cdot K^{-1}$)	100	[44]
ΔG_β ($kJ \cdot mol^{-1}$)	200	[42]	ρ_m ($kg \cdot m^{-3}$)	4.42×10^3	[45]

Fig. 9 shows the calculated temperature at the primary deformation region of the seven microgrooves. The average temperature almost shows linear elevation from 150 to 600 ℃ with the cutting speeds increasing from 62.83 to 439.82 mm/s.

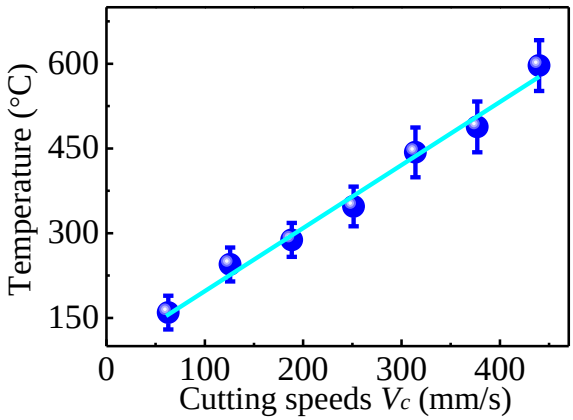

Fig. 9 Temperature evolution with cutting speed in the machining of Ti6Al4V alloys

Though the temperature increases with cutting speeds, the highest temperature is estimated to be about 641.78 °C, which is quite below the β phase transformation temperature (about 994 °C) of the Ti6Al4V alloy [35]. Therefore, β grains might coarsen with the increasing of temperature due to the obtained energy, but no phase transformation from α to β phase was expected to occur in the machining of all grooves.

The microstructure obtained from the serrated chip and microgroove of the seventh groove verifies that no phase transformation occurs during the machining process, as shown in Fig. 10 (a)-(d). Fig. 10 (c) and (d) show the microstructures obtained from the magnifying morphology (rectangular mark) in Fig. 10 (a) and from the seventh grooves, respectively. It is seen that both microstructures are also composed of the α phase and β particles, and no secondary α phase or lamellar α phase transformed from the β phase is observed in the morphology, which demonstrates that no phase transformation from (α + β) to the single β phase occurs during the groove machining process. By comparing Fig. 10 (a) and (b), numerous reticulate patterns are observed in the free surface of serrated chips, which are

supposedly induced by the erosion of many serrated chip segments after chemical etching.

Furthermore, the average size of β particles in the serrated chips is much smaller in comparison to the original microstructures, while the β grains in the groove surface were coarsened. In the machining process, chips are usually experienced high strain and strain rate, so grains are likely to be smashed into small grains [46]. Besides, a large number of dislocations induced by the severe plastic deformation could be accumulated in the serrated chips, and recrystallization of grains is likely to occur with the cutting temperature increase. Grain refinement in the cutting chips has been observed in the machining of copper, aluminium and titanium alloys [47-49]. However, grain growth instead of refinement of the β phase is obtained in the groove surface due to the increase of temperature, which is in agreement with the Eq. (20) that the volume fraction of α phase decrease but β phase increases with the temperature.

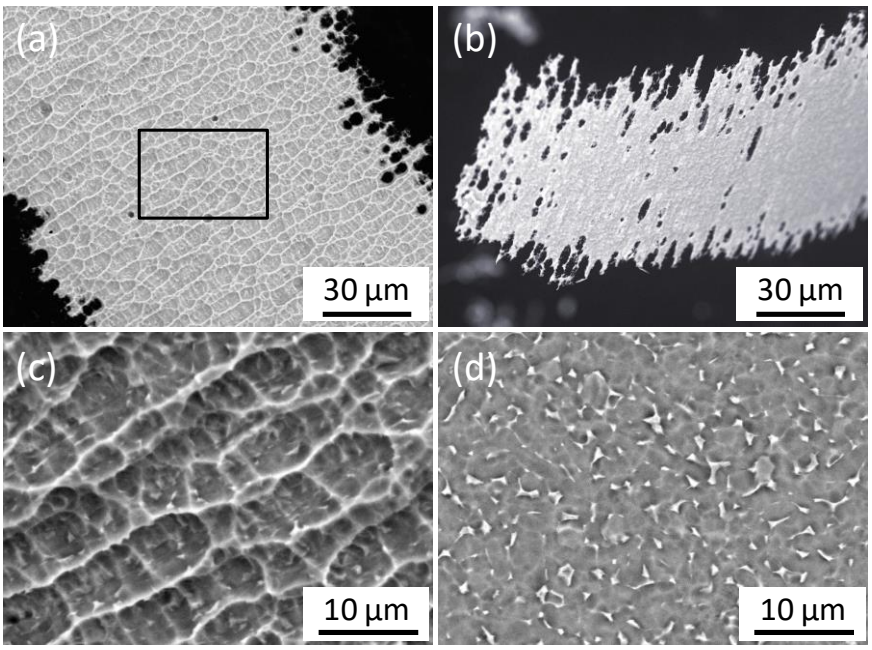

Fig. 10 SEM morphologies of the (a) free surface and (b) machined surface of the 7th serrated chip after chemical etching; microstructures from (c) the magnifying free surface marked in (a) and (d) the seventh groove after machining.

4.4 Cutting force verification

Fig. 11 (a) compares the cutting forces of the seven grooves from the measurement and models. Error bands of the measured and calculated cutting forces are given by the pink and green shadow areas, respectively. Both results indicate that the cutting force slightly increases with the cutting speeds. The average forces rise from about 2.38 to 2.55 N and from about 2.34 to 2.64 N for the measurement and calculation, respectively. Hence, the error of the models is in a range of 3.53 %. Besides, the calculated results from the model are in good agreement with the experimental forces at cutting speeds smaller than 251.33 mm/s, while the calculated forces show slight large values at high cutting speeds.

The contribution to the cutting forces is shown in Fig. 11 (b). It is seen that the normal force contribute significantly to the cutting force, which accounts for more than 60 % of the cutting force for all grooves. Especially for the seventh groove with a cutting speed of 439.82 mm/s, the percentage could reach as high as 73.51 %. In contrast, the frictional force between the diamond tool and serrated chips contributes little to the cutting force in machining all microgrooves.

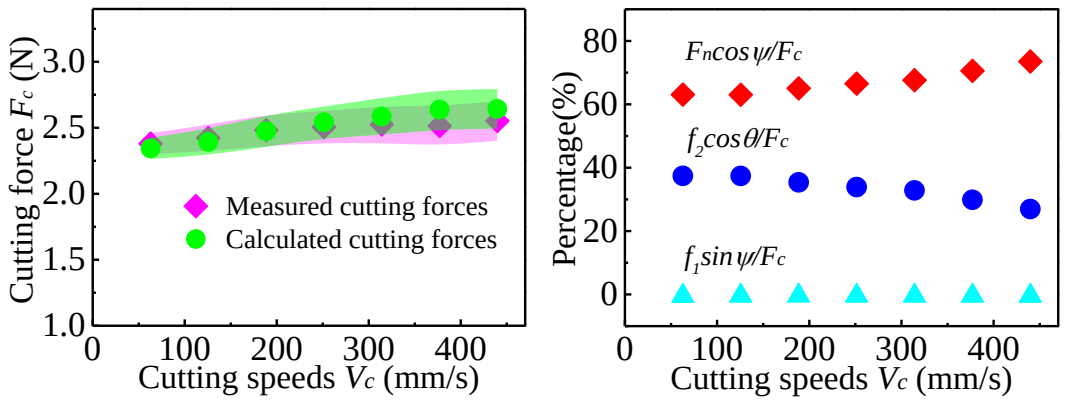

Fig. 11 The cutting force evolution and contributions to the cutting force with the cutting speeds, (a) Measured and calculated cutting forces and (b) contributions of normal and frictional forces to the cutting force at various cutting speeds

According to Eq. 6, the generation of the normal force is mainly attributed to the internal force to overcome the shear deformation of the Ti6Al4V workpiece. The internal force and equivalent stress at various cutting speeds are illustrated in Fig. 12, which show upward trends with the cutting speeds at the same DoC of 5 μm. The equivalent stress increases from about 410 to 660 MPa as the cutting speed rises from 62.83 to 439.82 mm/s. The temperature increase with the cutting speeds and an increase of temperature usually results in a reduction of plastic deformation resistance, so the sum of thermal and athermal stresses required to overcome plastic deformation should be reduced with the speeds. However, the equivalent stress in machining not only includes thermal and athermal stresses but also contains a dislocation drag stress based on Eq. 11. The sum of thermal and athermal stress indeed decreases with the cutting speeds, while the dislocation drag stress gradually increases with the cutting speeds due to the significant elevation of strain rates in machining, as shown in Fig. 12 (c). Therefore, the equivalent stress gradually increases with the cutting speeds.

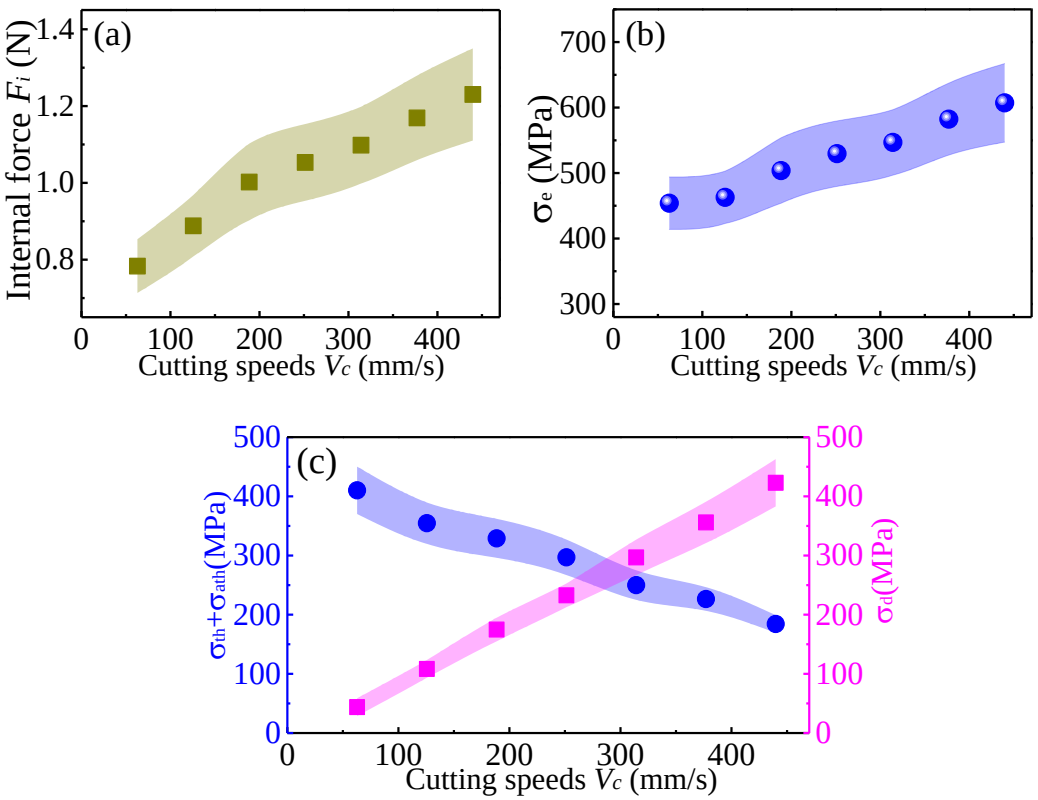

Fig. 12 Internal forces and stresses evolution with the cutting speeds, (a) internal forces, (b) equivalent stresses and (c) stresses attributed to the thermal, athermal and dislocation drag stresses

4.5 Material spring back analyses

4.5.1 DoC effects on material spring back

As the DoC is gradually increased to 5 μm, the width of a certain groove should also vary with depths for the groove being machined by the circular diamond cutting tool. Six groove widths ranging from 100 to 200 μm with an interval of 20 μm are used to explore the effects of DoC on material spring back. Since the cutting grooves show similar features, the middle groove (the 4th groove) is selected as an example to analyze the depth influence on spring back behaviour.

Fig. 13 (a) illustrates the ideal profiles of the cutting grooves at widths from 100

to 200 μm, corresponding to ideal depths of 1.125, 1.620, 2.205, 2.881, 3.648, 4.506 μm, respectively. Fig. 13 (b) shows the measured groove profiles at the same widths. The profiles show slightly fluctuation due to the unavoidable waviness on diamond cutting edges induced by the fabricating process [16]. The material spring back would contribute to shallow groove depths in comparison to the ideal depths, and values of measured depths at groove widths from 100 to 200 μm with an interval of 20 μm are about 0.724, 1.214, 1.793, 2.152, 2.526, 3.359 μm, respectively. Fig. 13 (c) shows the differences between the ideal and measured depths of cut at various groove widths. It is clearly seen that the difference increases slightly at DoC smaller than about 2.205 μm, and then increases significantly to about 1.124 μm at depths of cut greater than 3.648 μm. This indicates that the amount of material spring back shows an upward trend with the increasing of depth. Increase in DoC could induce more deformation of the workpiece, giving rise to more elastic deformation accumulated in the cutting zone. Hence, the spring back amount is higher at large depth. This is similar to the situation in sheet metal bending process that the spring back angles rise with bending angles if other parameters are the same [4, 50]. In addition, the reduction of Young's modulus with temperature is small at low DoC, so the spring back amount has little different. However, the Young's modulus reduces significantly at the large depth because of an obvious temperature increase, as shown in Fig. 13 (d). Besides, the large increase of DoC results in more heat accumulated in the cutting regions due to the low thermal conductivity of titanium alloy workpiece, giving rise to significant temperature rise in the deformation zone, which also contributes to high spring back.

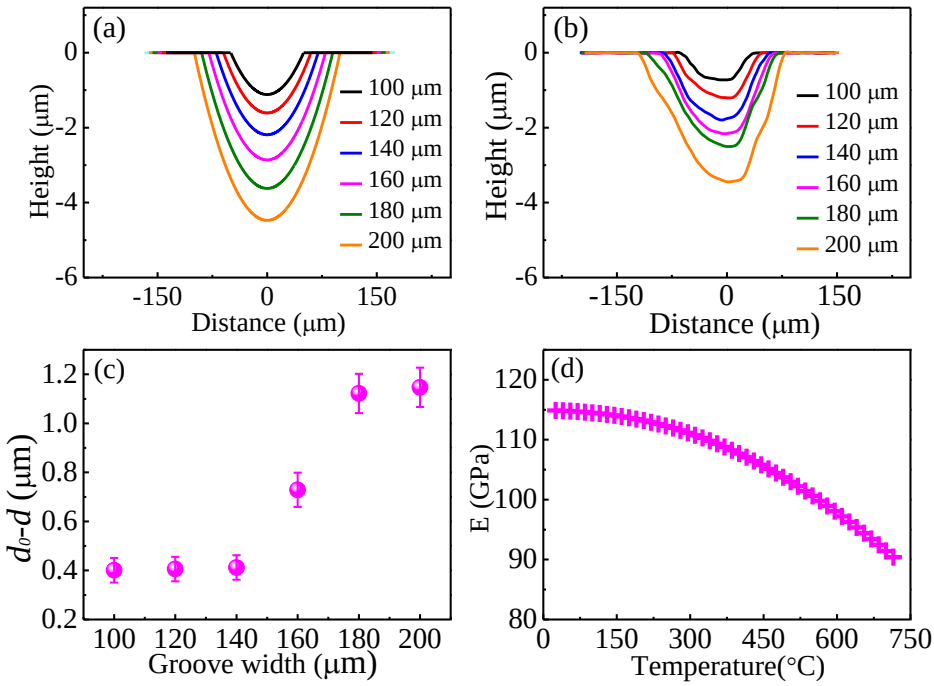

Fig. 13 Cross-sectional profiles for the (a) ideal and (b) measured groove surfaces; (c) differences between the ideal and measured depths at various groove width, and (d) influence of temperature on the Young's modulus

4.5.2 Cutting speed effects on material spring back

Fig. 14 compares profiles of the seven ideal and measured grooves at various radii with the same DoC of 5 μm. The profiles are not fully symmetrical along the curve centre due to the tool setting error, but it has no effect on analyzing the material spring back which could be clearly observed by comparing the depth difference between ideal and measured curves. As shown in the magnifying figure given in Fig. 14 (a), the measured depth gradually increases with the radius, which indicates that the amount of spring back shows a downward trend with the increasing of cutting speeds. Fig. 14 (b) shows the height differences between the measured and ideal depth of the seven microgrooves with various cutting speeds. Increase in cutting speed could result in a low spring back amount at the same DoC of 5 μm, which is in

accordance with the variation of materials spring back forces at different cutting speeds. In other words, a minor amount of material recovery corresponds to a small spring back force.

Based on Eq. (1), the thrust force is primarily determined by the spring back force, two frictional forces, the normal force, the front clearance angle and equivalent contact angle. Fig. 14 (d) compares different terms in Eq. (1) contributing to the thrust force evolution. It is seen that more than 45% of the thrust force is derived from the spring back force, and the fraction increases with the decreasing of cutting speeds. About 63.74% of the thrust force is induced by the spring back force at the smallest cutting speed of 62.83 mm/s. The left is from the two frictional forces and normal force by considering the front clearance angle and equivalent contact angle. Therefore, the spring back force is one of important part on the contribution of the thrust force in ultraprecision machining of Ti6Al4V alloys.

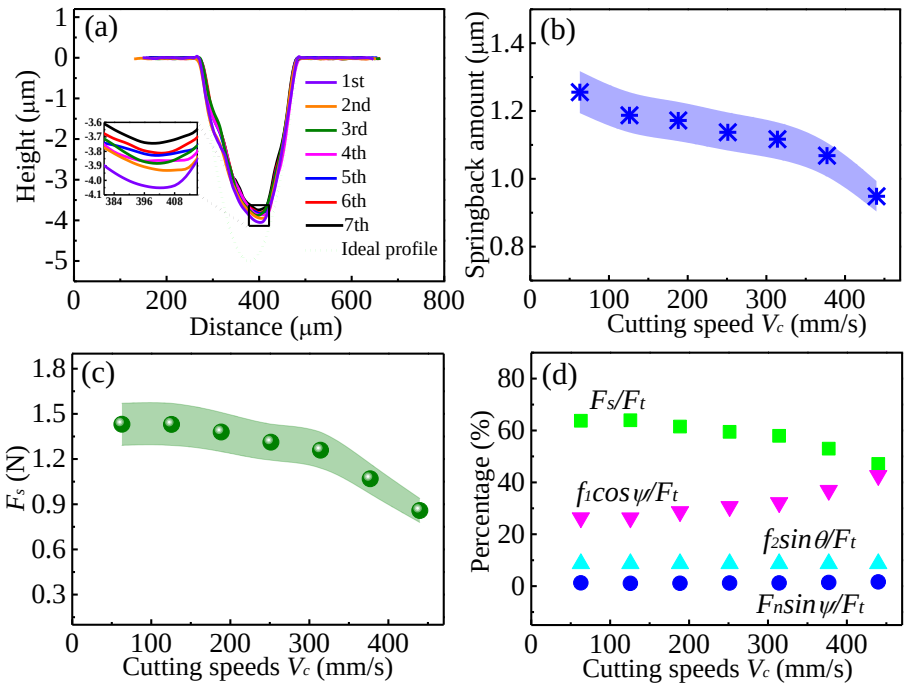

Fig. 14 Cutting speed effects on material spring back, (a) cross-sectional profiles of

seven cutting grooves and the ideal groove; effects of cutting speeds on (b) spring back amount and (c) spring back forces; (d) four factors contributing to the thrust force at various cutting speeds

5. Conclusion

The material cutting forces and spring back behaviour of the Ti6Al4V alloy are theoretically and experimentally investigated in ultraprecision machining of seven microgrooves with respect to material constitutive models and geometrical relationship, and conclusions are drawn as follows:

(i) Continuous serrated chips could be observed at cutting speeds ranging from 63 mm/s to 440 mm/s, and the height and width of serrated chip segments significantly vary with cutting speeds.

(ii) The cutting temperature is predicted to be increased with the increasing of cutting speeds. The largest estimated temperature could reach about 641.78 °C at the speed of 440 mm/s, which is lower than the β phase transformation temperature. This indicates that no phase transformation from α to β phase was expected to occur in the groove machining process, which was verified by the phase composition in the seventh cutting chip and groove after machining.

(iii) The average experimental and modelled cutting forces increase from about 2.38 to 2.55 N and from about 2.34 to 2.64 N, respectively. Hence, the calculated results from the model are in good agreement with the experimental forces within an error of about 3.53 %. Though the temperature rising with the cutting speeds could reduce the thermal and athermal stresses, the equivalent stress to overcome plastic deformation

increases with the cutting speeds due to the enhanced dislocation drag stress.

(iv) Increase in DoC and decrease in cutting speed would result in more material spring back during micro groove machining due to the evolution of the Young's modulus and spring back force. Besides, though the thrust force is affected by spring back force, frictional forces and the normal force, more than 45% of the thrust force is contributed from the spring back force.

Acknowledges

The work described in this paper was jointly supported by the Research Committee (Project No. G-YBLE) and Partner State Key Laboratory of Ultra-precision Machining Technology (Project No. RUWB) of the Hong Kong Polytechnic University.

References

[1] J. Mayeur, D. McDowell. A three-dimensional crystal plasticity model for duplex Ti–6Al–4V. Int J Plasticity 2007; 23:1457-1485.

[2] H.Y. Yu. Variation of elastic modulus during plastic deformation and its influence on springback. Mater Design 2009; 30:846-850.

[3] N. Duc-Toan, Y. Seung-Han, J. Dong-Won, B. Tien-Long, K. Young-Suk. A study on material modeling to predict spring-back in V-bending of AZ31 magnesium alloy sheet at various temperatures. Int J Adv Manuf Tech 2012; 62:551-562.

[4] Z. Jiang, H. Yang, M. Zhan, X. Xu, G. Li. Coupling effects of material properties and the bending angle on the springback angle of a titanium alloy tube during numerically controlled bending. Mater Design 2010; 31:2001-2010.

[5] J. Rychlewski. On Hooke's law. J Appl Math Mech 1984; 48:303-314.

[6] J. Liu, M. Fu, J. Lu, W. Chan. Influence of size effect on the springback of sheet metal foils in micro-bending. Comp Mater Sci 2011; 50:2604-2614.

[7] Z. Xu, L. Peng, E. Bao. Size effect affected springback in micro/meso scale bending process: Experiments and numerical modeling. J Mater Process Tech 2018; 252:407-420.

[8] A. Pramanik. Problems and solutions in machining of titanium alloys. Int J Adv Manuf Tech 2014; 70:919-928.

[9] E. Chiappini, S. Tirelli, P. Albertelli, M. Strano, M. Monno. On the mechanics of chip formation in Ti–6Al–4V turning with spindle speed variation. Int J Mach Tool Manu 2014; 77:16-26.

[10] C. Friedrich, V. Kulkarni. Effect of workpiece springback on micromilling forces. Microsyst Technol 2004; 10:472-477.

[11] I. Kang, J. Kim, J. Kim, M. Kang, Y. Seo. A mechanistic model of cutting force in the micro end milling process. J Mater Process Tech 2007; 187:250-255.

[12] Q. Zhao, B. Guo, H. Yang, X. Zhang, A mechanistic cutting force model for diamond fly-cutting of microstructured surface, in: 4th International Symposium on Advanced Optical Manufacturing and Testing Technologies: Advanced Optical Manufacturing Technologies, International Society for Optics and Photonics, 2009, pp. 728204.

[13] G. Zhang, S. To, S. Zhang. Relationships of tool wear characteristics to cutting mechanics, chip formation, and surface quality in ultra-precision fly cutting. Int J Adv

Manuf Tech 2016; 83:133-144.

[14] M. Kong, W. Lee, C. Cheung, S. To. A study of materials swelling and recovery in single-point diamond turning of ductile materials. J Mater Process Tech 2006; 180:210-215.

[15] S. To, C. Cheung, W. Lee. Influence of material swelling on surface roughness in diamond turning of single crystals. Mater Sci Tech 2001; 17:102-108.

[16] C. He, W. Zong, T. Sun. Origins for the size effect of surface roughness in diamond turning. Int J Mach Tool Manu 2016; 106:22-42.

[17] M.E. Merchant. Mechanics of the metal cutting process. I. Orthogonal cutting and a type 2 chip. J Appl Phys 1945; 16:267-275.

[18] C. Arcona, T.A. Dow. An empirical tool force model for precision machining. J Manuf Sci Eng 1998; 120:700-707.

[19] X. Zhang, M. Arif, K. Liu, A.S. Kumar, M. Rahman. A model to predict the critical undeformed chip thickness in vibration-assisted machining of brittle materials. Int J Mach Tool Manu 2013; 69:57-66.

[20] M.B. Jun, X. Liu, R.E. DeVor, S.G. Kapoor. Investigation of the dynamics of microend milling—part I: model development. J Manuf Sci Eng 2006; 128:893-900.

[21] J. Manjunathaiah, W. Endres. A study of apparent negative rake angle and its effect on shear angle during orthogonal cutting with edge-radiused tools. Trans N Amer Manufac 2000; 197-202.

[22] A.C. Ramos, H. Autenrieth, T. Strauß, M. Deuchert, J. Hoffmeister, V. Schulze. Characterization of the transition from ploughing to cutting in micro machining and

evaluation of the minimum thickness of cut. J Mater Process Tech 2012; 212:594-600.

[23] P. Huang, W. Lee. Cutting force prediction for ultra-precision diamond turning by considering the effect of tool edge radius. Int J Mach Tool Manu 2016; 109:1-7.

[24] N. Fang. Slip-line modeling of machining with a rounded-edge tool—Part I: new model and theory. J Mech Phys Solids 2003; 51:715-742.

[25] X. Jin, Y. Altintas. Slip-line field model of micro-cutting process with round tool edge effect. J Mater Process Tech 2011; 211:339-355.

[26] Z. Zhu, S. To, W.-L. Zhu, P. Huang, X. Zhou. Cutting forces in fast-/slow tool servo diamond turning of micro-structured surfaces. Int J Mach Tool Manu 2019; 136:62-75.

[27] Z. Sun, S. To, S. Wang. An analytical force model for ultra-precision diamond sculpturing of micro-grooves with textured surfaces. Int J Mech Sci 2019.

[28] A. Toropov, S.-L. Ko. Prediction of tool-chip contact length using a new slip-line solution for orthogonal cutting. Int J Mach Tool Manu 2003; 43:1209-1215.

[29] S.M. Son, H.S. Lim, J.H. Ahn. Effects of the friction coefficient on the minimum cutting thickness in micro cutting. Int J Mach Tool Manu 2005; 45:529-535.

[30] S.N. Melkote, R. Liu, P. Fernandez-Zelaia, T. Marusich. A physically based constitutive model for simulation of segmented chip formation in orthogonal cutting of commercially pure titanium. CIRP Ann 2015; 64:65-68.

[31] U. Kocks. Laws for work-hardening and low-temperature creep. J Eng Mater Tech 1976; 98:76-85.

[32] H. Mecking, U. Kocks. Kinetics of flow and strain-hardening. Acta Metall 1981;

29:1865-1875.

[33] T. Özel, E. Zeren. A methodology to determine work material flow stress and tool-chip interfacial friction properties by using analysis of machining. J Manuf Sci Eng 2006; 128:119-129.

[34] J. Luo, M. Li, X. Li, Y. Shi. Constitutive model for high temperature deformation of titanium alloys using internal state variables. Mech Mater 2010; 42:157-165.

[35] X. Fan, H. Yang. Internal-state-variable based self-consistent constitutive modeling for hot working of two-phase titanium alloys coupling microstructure evolution. Int J Plasticity 2011; 27:1833-1852.

[36] G. Kibria, B. Sarkar, B. Pradhan, B. Bhattacharyya. Comparative study of different dielectrics for micro-EDM performance during microhole machining of Ti-6Al-4V alloy. Int J Adv Manuf Tech 2010; 48:557-570.

[37] T.L. Bergman, F.P. Incropera, A.S. Lavine, D.P. DeWitt, Introduction to heat transfer, John Wiley & Sons, 2011.

[38] S.B. Giddings. Hawking radiation, the Stefan–Boltzmann law, and unitarization. Phys Lett B 2016; 754:39-42.

[39] W. Zong, T. Sun, D. Li, K. Cheng, Y. Liang. FEM optimization of tool geometry based on the machined near surface's residual stresses generated in diamond turning. J Mater Process Tech 2006; 180:271-278.

[40] N. Kotkunde, A.D. Deole, A.K. Gupta, S.K. Singh. Comparative study of constitutive modeling for Ti–6Al–4V alloy at low strain rates and elevated temperatures. Mater Design 2014; 55:999-1005.

[41] G. Sutter, G. List. Very high speed cutting of Ti–6Al–4V titanium alloy–change in morphology and mechanism of chip formation. Int J Mach Tool Manu 2013; 66:37-43.

[42] R. Picu, A. Majorell. Mechanical behavior of Ti–6Al–4V at high and moderate temperatures—Part II: constitutive modeling. Mat Sci Eng A 2002; 326:306-316.

[43] D. Umbrello. Finite element simulation of conventional and high speed machining of Ti6Al4V alloy. J Mater Process Tech 2008; 196:79-87.

[44] J.R. Howell, M.P. Menguc, R. Siegel, Thermal radiation heat transfer, CRC press, 2010.

[45] J. Yang, S. Sun, M. Brandt, W. Yan. Experimental investigation and 3D finite element prediction of the heat affected zone during laser assisted machining of Ti6Al4V alloy. J Mater Process Tech 2010; 210:2215-2222.

[46] Z. Zhao, S. To. An investigation of resolved shear stress on activation of slip systems during ultraprecision rotary cutting of local anisotropic Ti-6Al-4V alloy: Models and experiments. Int J Mach Tool Manu 2018; 134:69-78.

[47] H. Ding, N. Shen, Y.C. Shin. Modeling of grain refinement in aluminum and copper subjected to cutting. Comp Mater Sci 2011; 50:3016-3025.

[48] S. Swaminathan, T. Brown, S. Chandrasekar, T. McNelley, W. Compton. Severe plastic deformation of copper by machining: microstructure refinement and nanostructure evolution with strain. Scripta Mater 2007; 56:1047-1050.

[49] Q. Shi, Y.Y. Tse, R.L. Higginson. Effects of processing parameters on relative density, microhardness and microstructure of recycled Ti–6Al–4V from machining

chips produced by equal channel angular pressing. Mat Sci Eng A 2016; 651:248-258.

[50] M. Zhan, Y. Wang, H. Yang, H. Long. An analytic model for tube bending springback considering different parameter variations of Ti-alloy tubes. J Mater Process Tech 2016; 236:123-137.